



**HAL**  
open science

# Robust and Bifunctional Electrodeposited NiCoCr Ternary Alloy for Alkaline Water Electrolysis

Jeffrey Tourneur, Corinne Lagrost, Bruno Fabre

► **To cite this version:**

Jeffrey Tourneur, Corinne Lagrost, Bruno Fabre. Robust and Bifunctional Electrodeposited NiCoCr Ternary Alloy for Alkaline Water Electrolysis. *Advanced Energy and Sustainability Research*, 2023, *Advanced Energy and Sustainability Research*, 5 (2), pp.2300133. 10.1002/aesr.202300133 . hal-04327347

**HAL Id: hal-04327347**

**<https://hal.science/hal-04327347v1>**

Submitted on 4 Nov 2024

**HAL** is a multi-disciplinary open access archive for the deposit and dissemination of scientific research documents, whether they are published or not. The documents may come from teaching and research institutions in France or abroad, or from public or private research centers.

L'archive ouverte pluridisciplinaire **HAL**, est destinée au dépôt et à la diffusion de documents scientifiques de niveau recherche, publiés ou non, émanant des établissements d'enseignement et de recherche français ou étrangers, des laboratoires publics ou privés.



Distributed under a Creative Commons Attribution 4.0 International License

# Robust and Bifunctional Electrodeposited NiCoCr Ternary Alloy for Alkaline Water Electrolysis

Jeoffrey Tourneur, Corinne Lagrost, and Bruno Fabre\*

Electrodeposited NiCoCr ternary alloy is explored as a cost-effective and Earth-abundant alternative electrocatalyst for hydrogen evolution reaction (HER) and oxygen evolution reaction (OER) in alkaline conditions. Different metal salt concentrations (between 10 and 100 mM) and cathodic current densities (between 75 and 225 mA cm<sup>-2</sup>) are tested to prepare an optimized material exhibiting both the best electrocatalytic efficiency and robustness for water splitting. Combining electrochemistry with complementary physicochemical characterizations (scanning electron microscopy, energy-dispersive X-ray spectroscopy analysis, and X-ray photoelectron spectroscopy) has enabled to gain a deep knowledge of the composition, morphology, and catalytic activity before and after long-term electrolytic tests. Compared with the related NiCo and NiCr binary alloys, NiCoCr shows catalytic performance for HER similar to NiCr and higher than that of NiCo. In contrast, its catalytic activity for OER is quite comparable to that of NiCo and higher than that of NiCr. Importantly, the presence of Cr is found to be beneficial to increase the oxidation resistance of the ternary alloy. This work provides a scalable way to produce bifunctional and robust electrode materials.

polluting process leading to the emission of greenhouse gases. The development of new routes toward the generation of carbon-free H<sub>2</sub> is a major challenge to be addressed for a successful hydrogen economy. In that context, the production of green H<sub>2</sub> by water electrolysis is an easily scalable electrochemical process but still expensive due to the scarcity and the cost of noble metals like Pt, Pd, Ir, or Ru used as electrodes in electrolyzers.<sup>[4]</sup> These metals are employed principally into proton exchange membrane electrolyzers in acid medium.<sup>[1,5]</sup> This medium leads to the highest current densities to produce H<sub>2</sub> but is very corrosive. As alternative technologies, anion exchange membrane electrolyzers show great promises because they allow the use of Earth-abundant and low-cost transition metals as electrocatalysts for both anode and cathode with an electrocatalytic efficiency competing with that of Pt group


## 1. Introduction

Worldwide energy consumption should increase about 60% from 2010 to 2040,<sup>[1]</sup> which has a strong environmental impact by threatening climate and causing global warming. Therefore, research needs to stay focused on finding new ways to produce and store energy. Hydrogen is an energy vector that is attracting growing interest because of its high mass energy density (123 MJ kg<sup>-1</sup>). Nowadays, it is used as a chemical reagent to desulfurize oil or produce ammoniac by Haber–Bosch process.<sup>[2]</sup> It is also an emerging fuel for mobility, and it could become a solution to store the excess of energy produced by intermittent and renewable sources of electricity.<sup>[3]</sup> Hydrogen is currently predominantly produced by steam reforming of methane, which is a

metals.<sup>[6]</sup> In that context, several reports have demonstrated the high efficiency and stability of Ni-based bimetallic electrocatalysts for both hydrogen evolution reaction (HER) and oxygen evolution reaction (OER) in alkaline medium.<sup>[7–10]</sup> In an effort to standardize the evaluation of the catalytic performance of such materials, Jaramillo and co-workers have previously reported a benchmarking study of numerous electrodeposited Ni-based binary alloys incorporating, for example, Co, Cr, Mo, Fe, La, or W.<sup>[11]</sup> These alloyed materials were easily and quickly prepared from the electrochemical reduction of the two corresponding metallic salts.<sup>[11,12]</sup> Other groups have also demonstrated that ternary alloys such as NiCoFe,<sup>[13,14]</sup> NiCoMo,<sup>[15,16]</sup> NiCrMo,<sup>[17]</sup> NiFeMo,<sup>[18,19]</sup> and NiFeCr<sup>[20]</sup> are excellent candidates for HER and OER. Mo arouses interest because of its high ability to adsorb protons while Ni can dissociate water.<sup>[21]</sup> The precise role of Fe is still under discussion, it could either act as an active site for the reaction or activate the reaction.<sup>[22,23]</sup> Co is known to catalyze HER and OER, while Cr is usually considered for its ability to effectively protect the catalytic alloy against corrosion.<sup>[24,25]</sup>

The aim of this work is to explore the possibility to improve both electrocatalytic efficiency and durability of NiCo and NiCr alloys by combining these three base metals in the form of a NiCoCr ternary alloy. This so-called medium-entropy alloy is well known for its outstanding mechanical properties and its irradiation resistance<sup>[26–28]</sup> but to date, it has never been tested for electrocatalytic purposes. Herein, such an alloy was prepared using a simple and convenient electrodeposition method from the electrochemical reduction of the corresponding metal salts.

J. Tourneur, C. Lagrost, B. Fabre  
CNRS, ISCR (Institut des Sciences Chimiques de Rennes) – UMR6226  
Univ Rennes  
F-35000 Rennes, France  
E-mail: bruno.fabre@univ-rennes1.fr

 The ORCID identification number(s) for the author(s) of this article can be found under <https://doi.org/10.1002/aesr.202300133>.

© 2023 The Authors. Advanced Energy and Sustainability Research published by Wiley-VCH GmbH. This is an open access article under the terms of the Creative Commons Attribution License, which permits use, distribution and reproduction in any medium, provided the original work is properly cited.

DOI: 10.1002/aesr.202300133

This novel catalytic material exhibits a bifunctional catalytic activity for OER and HER in alkaline solution and its performance metrics is compared to those of the related binary alloys.

## 2. Results and Discussion

### 2.1. Preparation and Characterization of NiCo, NiCr, and NiCoCr on Nickel Foam Substrates

The catalytic alloys were prepared from the electrochemical reduction of the corresponding metal cations (in the form of  $\text{NiCl}_2$ ,  $\text{CoCl}_2$ , and  $\text{CrCl}_3$ ) on nickel foam (NF). In order to obtain an homogeneous deposit, a crystal modifier (ethylenediamine dihydrochloride) was added.<sup>[13]</sup> Different metal chloride concentrations (between 10 and 100 mM) and cathodic current densities (between 75 and 225  $\text{mA cm}^{-2}$ ) have been tested and these experimental parameters were optimized in order to produce a film that strongly adhered to NF and not impair its porosity (Table S1, Supporting Information). Moreover, sufficiently high current densities were required to promote the electrodeposition of Cr from  $\text{Cr}^{3+}$  due to the highly negative redox potential of the couple  $\text{Cr}^{3+}/\text{Cr}$  with respect to  $\text{Ni}^{2+}/\text{Ni}$  and  $\text{Co}^{2+}/\text{Co}$ :  $E^\circ(\text{Cr}^{3+}/\text{Cr}) = -0.74 \text{ V}$  versus reversible hydrogen electrode (RHE),  $E^\circ(\text{Ni}^{2+}/\text{Ni}) = -0.25 \text{ V}$  versus RHE, and  $E^\circ(\text{Co}^{2+}/\text{Co}) = -0.28 \text{ V}$  versus RHE.<sup>[29]</sup> Globally, such characteristics were obtained by applying a moderate current density (75  $\text{mA cm}^{-2}$ ) for a long period (10 min) in a diluted metal salt bath. When a high current density was applied ( $>150 \text{ mA cm}^{-2}$ ), a crust immediately formed and closed pores of NF (as shown in Figure S1, Supporting Information, for NiCoCr). If the electrodeposition time was too short (1 min), no deposit was observed even at a high metal salt concentration (Figure S1, Supporting

Information). During the electrodeposition process, hydrogen bubbles were released and could structure the deposit as a porous template<sup>[30]</sup> (Figure S2, Supporting Information).

The morphological and microstructural characteristics of the different optimized alloys were evaluated by scanning electron microscopy (SEM) and energy-dispersive X-ray spectroscopy (EDX) (Figure 1). All the electrodeposited materials homogeneously covered the NF support. However, it is worth noticing that the Cr-containing films showed some cracks which were absent in the structure of NiCo. It is anticipated that such an aerated structure should facilitate the removal of  $\text{H}_2$  and  $\text{O}_2$  gas bubbles during electrolytic HER and OER tests, respectively. Moreover, the EDX analysis confirmed the presence of the expected metal elements which were uniformly distributed on NF (Figure 1j–l and S3–S5, Supporting Information). We also note the presence of Cl for all samples (with an average content lower than 3 at%) probably coming from the chloride salts used for electrodeposition.

The X-Ray diffraction (XRD) patterns of the optimized alloy-coated NF samples are shown in Figure S6, Supporting Information. Only the peaks assigned to different Ni forms, namely, Ni(111), Ni(200), and Ni(220), were visible for all samples at  $\approx 44.6^\circ$ ,  $51.9^\circ$ , and  $76.4^\circ$ , respectively. Furthermore, any distinct Co and Cr peaks were not observed in the spectra. Such a result is not surprising and is common for electrodeposited binary or ternary Ni alloys.<sup>[13,18]</sup> However, a careful examination of these spectra showed a slight shift of the Ni(111) peak position to lower angles for NiCoCr as compared to those of NiCo and NiCr, 44.5 versus  $44.6^\circ$ . This downshift in  $2\theta$  observed for NiCoCr was thought to be caused by the incorporation of the larger Cr atoms (atomic radius: 0.166 nm) in the alloy while no significant shift of the spectrum was observed for NiCo due to similar radii of the Ni (0.149 nm) and Co (0.152 nm) atoms.

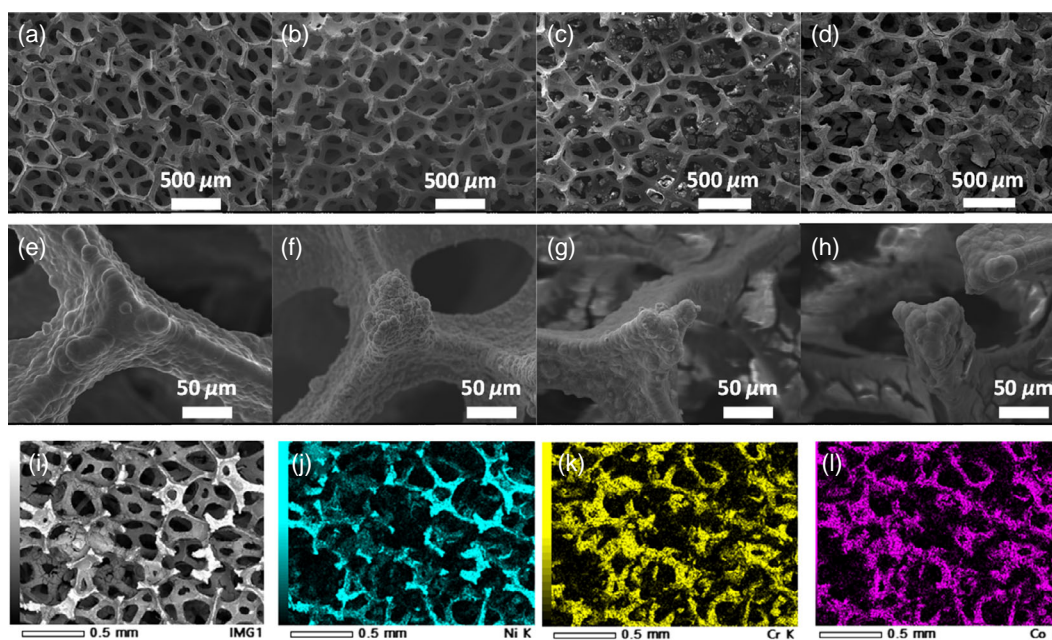


**Figure 1.** SEM images at a–d) low and e–h) higher magnifications of a,e) bare NF, b,f) NiCo, c,g) NiCr, and d,h) NiCoCr electrodeposited on NF. EDX mapping of i–l) NiCoCr showing the homogeneous distribution of Ni (j, blue), Cr (k, yellow), and Co (l, pink).

The surface composition of the samples was probed by X-ray photoelectron spectroscopy (XPS). For all materials, the survey spectra displayed the characteristic peaks corresponding to the expected elements, namely, Ni, Co, Cr, and O (Figure S7, Supporting Information). The presence of adventitious C, Cl, and N was also detected for the three materials at comparable levels, probably coming from ethylenediamine dihydrochloride in the electrodeposition bath. The atomic ratios Co/Ni and Cr/Ni were evaluated from the XPS survey spectra (Table S2,

Supporting Information). They were in the range 0.73–1.26 and were rather consistent with an equiatomic metal stoichiometry in the alloy. High-resolution core-level spectra for Ni2*p*, Co2*p*, and Cr2*p* were recorded and peak-fitted to show the chemical states of the different metallic elements (Figure 2). The high-resolution spectra of Ni2*p* exhibited the characteristic doublet structure of Ni2*p*<sub>3/2</sub> and Ni2*p*<sub>1/2</sub> with an energy separation of 17.6 eV due to spin–orbit splitting. A careful peak fitting of the Ni2*p*<sub>3/2</sub> component was performed since identical

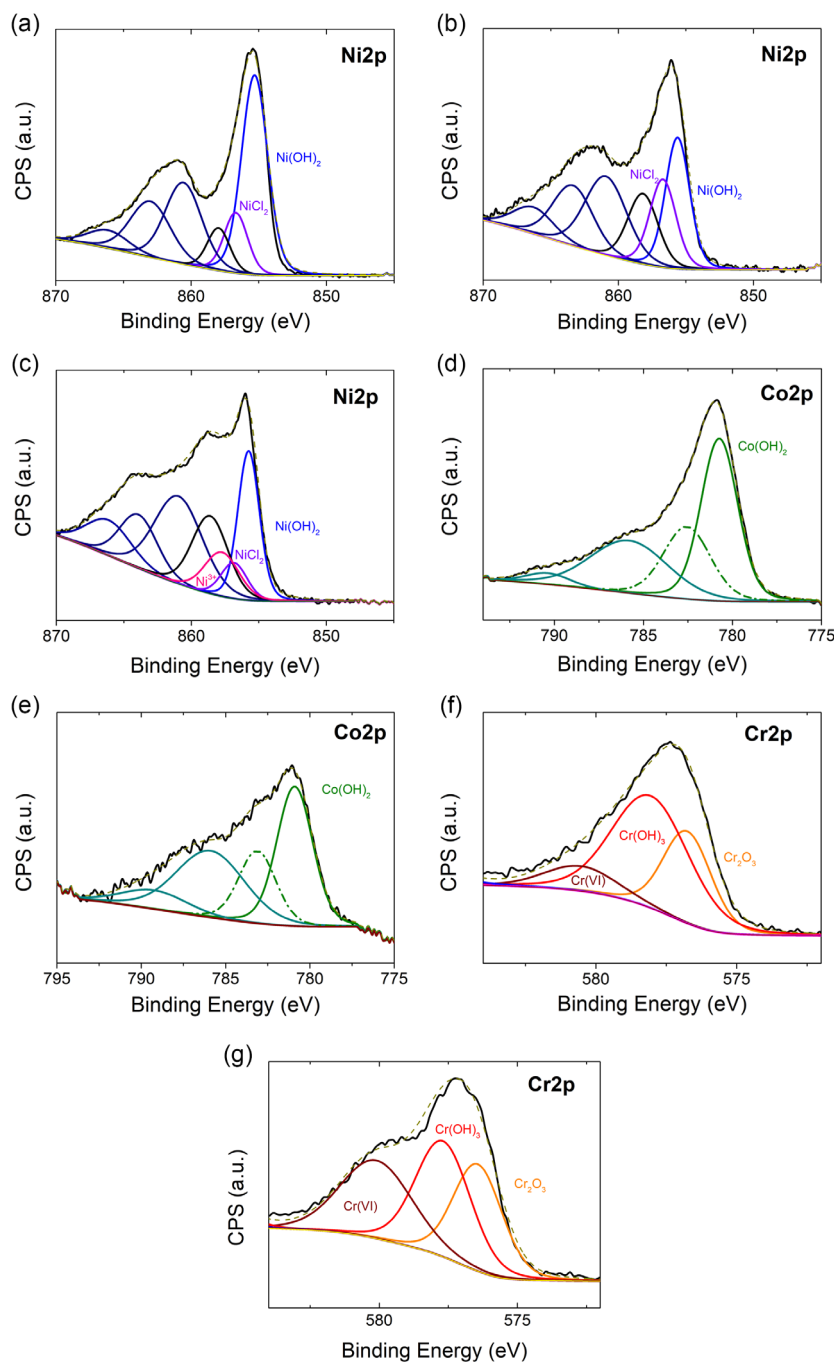


**Figure 2.** Peak-fitted high-resolution core-level spectra for the a–c) Ni2*p*<sub>3/2</sub>, d,e) Co2*p*<sub>3/2</sub>, and f,g) Cr2*p*<sub>3/2</sub> regions of a,d) NiCo, b,f) NiCr, and c,e,g) NiCoCr.

information could be drawn for the other  $Ni2p_{1/2}$  component (Figure 2a–c). The peaks for the three catalytic materials could be fitted with two  $Ni^{II}$  components at  $855.6 \pm 0.2$  eV and  $856.8 \pm 0.2$  eV and associated with their usual satellites peaks at  $\approx 861.0$ ,  $863.5$ , and  $866.5$  eV.<sup>[31–33]</sup> The main contribution at  $855.6 \pm 0.2$  eV corresponds to  $Ni(OH)_2$  while the second smallest one (5–15%) is probably due to the presence of residual  $NiCl_2$  salt used for electrodeposition (Table S3, Supporting Information) following analyses in previous works.<sup>[31–35]</sup> In addition, a small contribution (less than 10%) of  $Ni^{3+}$  at  $857.5$  eV could be also detected for the NiCoCr material that might arise from surface oxidation of  $Ni(OH)_2$  upon exposure to air.<sup>[34]</sup> Note that an additional peak at  $858.2 \pm 0.4$  eV was also used to model the valley between main peaks and satellites, corresponding to the inter-band loss of energy.<sup>[36,37]</sup> The high-resolution  $Co2p$  spectra showed the typical spin–orbit splitting into two components  $Co2p_{3/2}$  and  $Co2p_{1/2}$ . Only the  $Co2p_{3/2}$  component was peak-fitted in order to elucidate the chemical nature of the materials. The  $Co2p_{3/2}$  spectra have a complex structure because of the coupling between the  $2p$  core-level hole and the high spin valence electrons, resulting in multiplet splitting. For both NiCo and NiCoCr, the spectra could be fitted with two peaks at  $780.7 \pm 0.2$  eV and  $782.6 \pm 0.2$  eV, corresponding to the envelopes of the multiplet splitting,<sup>[38]</sup> and two broad satellite peaks at higher binding energy ( $786.3 \pm 0.3$  eV and  $790.5 \pm 0.4$  eV) (Figure 2d,e). Such a curve fitting fully agrees with the presence of  $Co(OH)_2$ , while the presence of other Co oxides or hydroxides, notably  $CoOOH$  ( $Co^{3+}$ ) could be discarded since peaks at lower binding energy and a different fingerprint for the satellites contribution are expected for these species.<sup>[39]</sup> The  $Cr2p$  spectra of NiCr and NiCoCr also consist of doublets due to spin–orbit coupling. The  $Cr2p_{3/2}$  was decomposed with three components (Figure 2f,g). The first signal at  $576.6 \pm 0.2$  eV could be ascribed to  $Cr_2O_3$ , while the two other ones at  $577.9 \pm 0.2$  eV and  $580.3 \pm 0.2$  eV corresponded to the contributions of  $Cr(OH)_3$  and  $Cr(VI)$  species, respectively.<sup>[31,33]</sup> From the peak areas, the relative concentrations of  $Cr_2O_3$ ,  $Cr(OH)_3$ , and  $Cr(VI)$  could be estimated to be  $\approx 0.3/0.6/0.1$  and  $0.3/0.4/0.3$  for NiCr and NiCoCr, respectively. It is worth noticing that the hexavalent chromium content was higher in NiCoCr than in NiCr. While  $Cr(III)$  tends to be readily oxidized to  $Cr(VI)$  by atmospheric oxygen, some studies reported that the presence of cobalt in a metal

alloy could promote the formation of  $Cr(VI)$  species in the layer.<sup>[40,41]</sup>

## 2.2. Electrocatalytic Activity for HER and OER

The electrocatalytic activity of the optimized NiCoCr was evaluated in alkaline medium (1.0 M KOH, pH 14) and compared with that of the bimetallic alloys prepared in this study, namely NiCo and NiCr, along with the reference bare NF.

As shown in Figure 3, a reversible redox wave corresponding to the formation and oxidation of nickel hydrides<sup>[42]</sup> was observed at 0.1 V versus RHE for the three Ni alloys. This wave was followed by the HER one starting below  $\approx -0.1$  V versus RHE. NiCoCr and NiCr exhibited the highest HER activity, as supported by the lowest  $iR$ -corrected overpotential values of 0.10 and 0.27 V measured at 10 ( $\eta_{10}$ ) and 100 ( $\eta_{100}$ )  $mA\ cm^{-2}$ , respectively (Table 1). These values were respectively 0.14 and 0.10 V lower than those determined for NF. Moreover, relatively close Tafel slopes were determined for all the studied electrodes, between  $\approx 96$  and 120 mV per decade (Figure 3b). Such values are indicative of a HER process controlled by the same reaction step, namely, the Volmer reaction that corresponds to the adsorption of hydronium ions onto the active sites of the catalysts.<sup>[43]</sup>

Regarding the oxidation region, a scan rate-dependent reversible redox wave ( $Ni^{3+}/Ni^{2+}$ ) was first observed for all materials between 1.2 and 1.6 V versus RHE, corresponding to the oxidation of Ni hydroxide to  $NiOOH$ <sup>[42,44]</sup> which is the catalytically active species for OER (Figure 4).<sup>[45,46]</sup> This peak was followed

**Table 1.** HER electrocatalytic parameters for different modified NF cathodes in 1 M KOH (pH 14).

Electrode	$\eta_{10}$ [V] <sup>a)</sup>	$\eta_{100}$ [V] <sup>a)</sup>	Tafel slope [mV dec <sup>-1</sup> ]
Bare NF	0.24	0.37	96
NiCo	0.20	0.33	118
NiCr	0.10	0.27	120
NiCoCr	0.11	0.27	109

<sup>a)</sup> Ohmic drop-corrected overpotential for a current density of 10 and 100  $mA\ cm^{-2}$ . The  $\eta_{10}$  values were determined from the backward scans in order to eliminate the contribution of the Ni hydrides-related redox wave in the cathodic current.

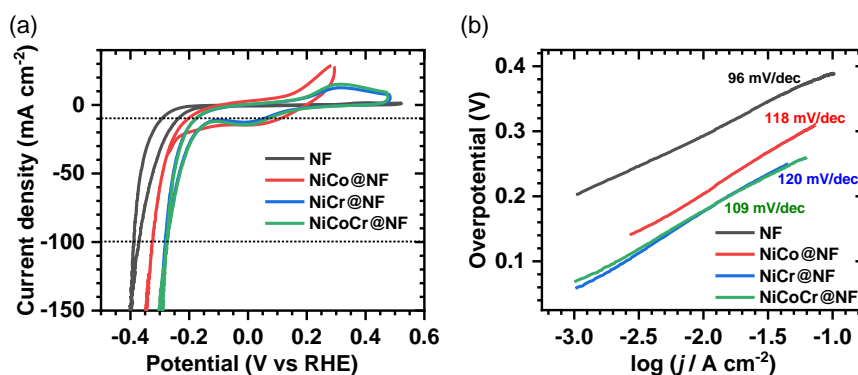


**Figure 3.** a)  $iR$ -corrected HER voltamperometric curves at  $20\ mV\ s^{-1}$  of bare NF and electrodeposited alloys in 1 M KOH solution and b) corresponding Tafel slopes. Note that a smaller scan rate of  $5\ mV\ s^{-1}$  yielded similar current densities for HER (Figure S8, Supporting Information).

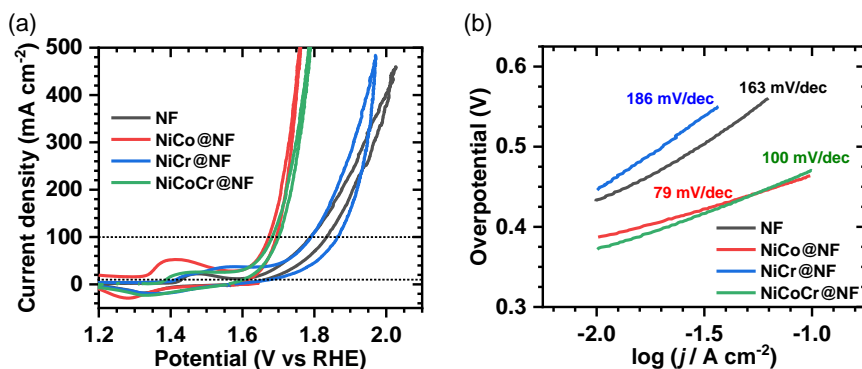


**Figure 4.** a) *iR*-corrected OER voltamperometric curves at  $20 \text{ mV s}^{-1}$  of bare NF and electrodeposited alloys in  $1 \text{ M KOH}$  solution and b) corresponding Tafel slopes. Note that a smaller scan rate of  $5 \text{ mV s}^{-1}$  yielded similar current densities for OER (Figure S8, Supporting Information).

by the OER signal displaying a much larger current density. NiCo and NiCoCr were found to exhibit the highest OER activity with close overpotential values  $\eta_{10}$  and  $\eta_{100}$  of 0.38 and 0.45 V, respectively (Table 2). These values were respectively 0.08 and 0.10 V lower than those determined for bare NF. Consistent with that, the Tafel slopes of 100 and  $79 \text{ mV dec}^{-1}$  determined for NiCoCr and NiCo, respectively, were smaller than those of the other prepared electrodes, with values between 163 and  $186 \text{ mV dec}^{-1}$  (Figure 4b).

In addition, because the electrode support is a porous material (namely, NF), we need to estimate the electrochemically active surface area (ECSA) for each tested electrode.<sup>[47]</sup> A commonly used approach is to determine the electrochemical double-layer capacitance ( $C_{dl}$ ) from cyclic voltammograms (CVs) monitored in a non-Faradaic region at different scan rates (Figure S9, Supporting Information, see the experimental section for details).  $C_{dl}$  is directly proportional to ECSA ( $\text{ECSA} = C_{dl}/C_s$  where  $C_s$  is the specific capacitance of flat Ni)<sup>[47]</sup> and is a good indicator of the density of electrocatalytically active sites. In line with other aforementioned electrochemical data, NiCoCr exhibited the largest  $C_{dl}$  value ( $2.5 \text{ mF cm}^{-2}$ , Figure 5) compared with the other electrodes, namely bare NF ( $0.4 \text{ mF cm}^{-2}$ ), NiCo ( $0.9 \text{ mF cm}^{-2}$ ), and NiCr ( $2.0 \text{ mF cm}^{-2}$ ).

### 2.3. Durability of the Electrodeposited Alloys for HER and OER

Apart from the electrocatalytic performance, the long-term stability of electrodeposited materials was also examined in harsh conditions at a constant current density of  $-100 \text{ mA cm}^{-2}$  (HER)

**Table 2.** OER electrocatalytic parameters for different modified NF anodes in  $1 \text{ M KOH}$  (pH 14).

Electrode	$\eta_{10} [\text{V}]^a$	$\eta_{100} [\text{V}]^a$	Tafel slope [ $\text{mV dec}^{-1}$ ]
NF	0.43	0.55	163
NiCo	0.39	0.44	79
NiCr	0.45	0.54	186
NiCoCr	0.37	0.45	100

<sup>a</sup> Ohmic drop-corrected overpotential for a current density of 10 and  $100 \text{ mA cm}^{-2}$ . The  $\eta_{10}$  values were determined from the backward scans in order to eliminate the contribution of the  $\text{Ni}^{3+}/\text{Ni}^{2+}$  redox wave in the anodic current.

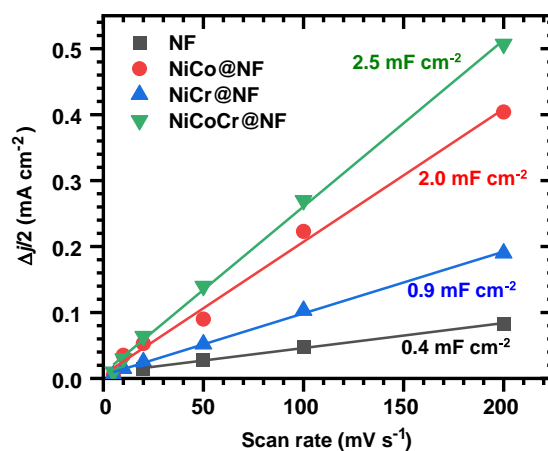


**Figure 5.** Determination of  $C_{dl}$  for the different electrodes from the  $\Delta j/2$  versus  $\nu$  plots where  $\Delta j$  is the difference between the anodic and cathodic charging current densities (taken from CVs shown in Figure S9, Supporting Information).

and  $+100 \text{ mA cm}^{-2}$  (OER) in  $1 \text{ M KOH}$  solution (Figure 6). For HER, the corresponding chronopotentiometric curves showed that NiCo, NiCr, and NiCoCr were stabilized at an overpotential in the range 0.28–0.31 V after 10 h electrolysis, in relatively good agreement with the potential values derived from the HER voltammetric curves (Figure 3a). Furthermore, NiCo was found to be the most robust since a potential change of only 3 mV was measured after 10 h electrolysis, while a potential change of 42, 51, and 115 mV was monitored for NiCr, NiCoCr, and bare NF, respectively. Concerning OER, NiCo and NiCoCr were stabilized at overpotentials of 0.40 and 0.44 V, respectively, which again were close to potential values derived from the OER voltammetric curves (Figure 4). Despite a slightly higher overpotential, it can be noticed that NiCoCr was the most robust material for OER with a potential change of only 1 mV after 10 h electrolysis, compared with values of 30, 70, and 100 mV measured for NiCr, NiCo, and bare NF, respectively. Such results demonstrate the beneficial effect of Cr to increase both corrosion and oxidation resistances of the metallic alloy.

The stability of NiCoCr has also been examined by potentiodynamic cycling. Figure 7 shows the electrochemical response of

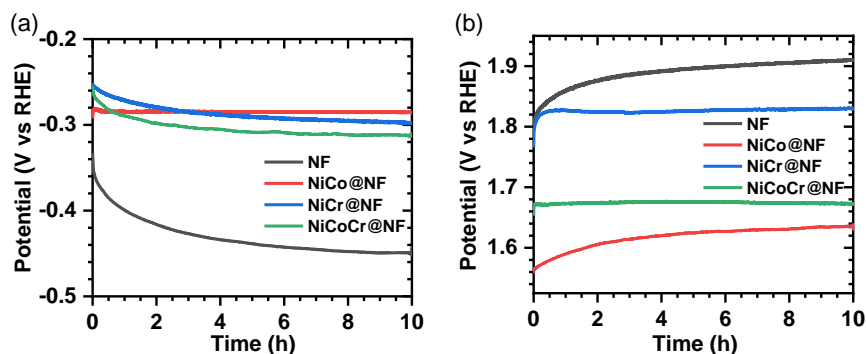


**Figure 6.** Chronopotentiometric curves of bare NF and the electrodeposited alloys at an applied current density of a)  $-100 \text{ mA cm}^{-2}$  and b)  $+100 \text{ mA cm}^{-2}$  in 1 M KOH.

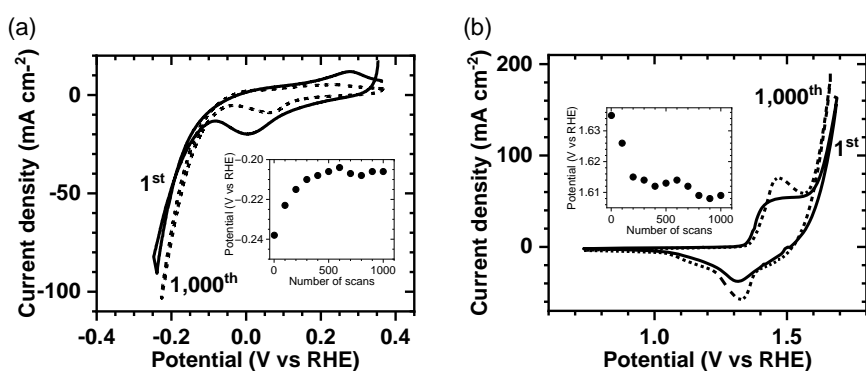


**Figure 7.**  $iR$ -corrected CVs at  $20 \text{ mV s}^{-1}$  of NiCoCr in 1 M KOH solution for a) HER and b) OER before (solid lines) and after 1000 consecutive cyclic voltammetry scans (dashed lines). The insets represent the variation of the potential arbitrarily measured at  $\pm 80 \text{ mA cm}^{-2}$  with the number of scans.

NiCoCr after 1,000 consecutive cyclic voltammetry scans for the cathodic (HER) and anodic (OER) parts. As previously observed for other Ni-based catalytic surfaces,<sup>[42,44]</sup> the electrochemical cycling led to a gradual improvement of the electrode performance, as supported by the decreased HER and OER overpotentials at the thousandth cycle. This so-called activation process took place until  $\approx 500$ th scan before reaching a situation where the potential was stabilized overall (insets in Figure 7).

The changes in the chemical composition of the catalytic materials after the controlled-current electrolytic tests were monitored by EDX and XPS. As shown in Figure S10, Supporting Information, the expected elements for the trimetallic alloy, namely, Ni, Co, and Cr, were still homogeneously distributed over NF. The EDX data and the XPS survey spectra (Figure S11, Supporting Information) also showed the presence of potassium (between 3 and 6 at%) for all materials after both the HER and OER stability tests. Adsorbed potassium ions from the electrolyte were commonly detected for Ni-based HER and OER catalysts when studied in alkaline KOH medium.<sup>[11]</sup> Interestingly, the atomic ratios Co/Ni and Cr/Ni extracted from the XPS survey spectra were found to be only slightly modified after HER electrolysis (Table S2, Supporting Information). Moreover, the average oxidation level of the three materials was not significantly modified (Table S4, Supporting Information). A careful examination of the high-resolution core-level spectra for Ni2p and Co2p showed still the presence of metal(II) hydroxide species ( $\text{Ni}(\text{OH})_2$

and  $\text{Co}(\text{OH})_2$ ) as the main contributions, without the emergence of a new phase (Figure 8). However, the contribution of  $\text{NiCl}_2$  decreased after long-term electrolysis, evidencing the release of  $\text{NiCl}_2$ . We also observed a very small contribution of metallic nickel at the catalyst surface in the case of NiCr, probably occurring during the reductive HER process (Table S3, Supporting Information). Concerning Cr2p, the postelectrolysis relative concentrations of  $\text{Cr}_2\text{O}_3$ ,  $\text{Cr}(\text{OH})_3$ , and Cr(VI) for NiCr were almost unchanged (0.4/0.5/0.1, Table S4, Supporting Information). In contrast, the values of 0.4/0.4/0.2 determined for NiCoCr were consistent with the loss of some Cr(VI) in the form of  $\text{CrO}_4^{2-}$  chromate species dissolved in the electrolyte solution, as previously reported by Peugeot et al. for NiFeCr electrodes.<sup>[48]</sup>

### 3. Conclusion

In this work, we report for the first time the electrocatalytic behavior of a NiCoCr trimetallic alloy. The catalytic material was directly prepared on NF from the electrochemical reduction of Co, Cr, and Ni metal salts in aqueous solution. Interestingly, the metallic components were found to be evenly distributed within the material, with almost an equiatomic composition, and covered homogeneously the NF support. The resulting material was shown to be electrocatalytically active for both HER and OER in alkaline medium. Compared with the electrodeposited

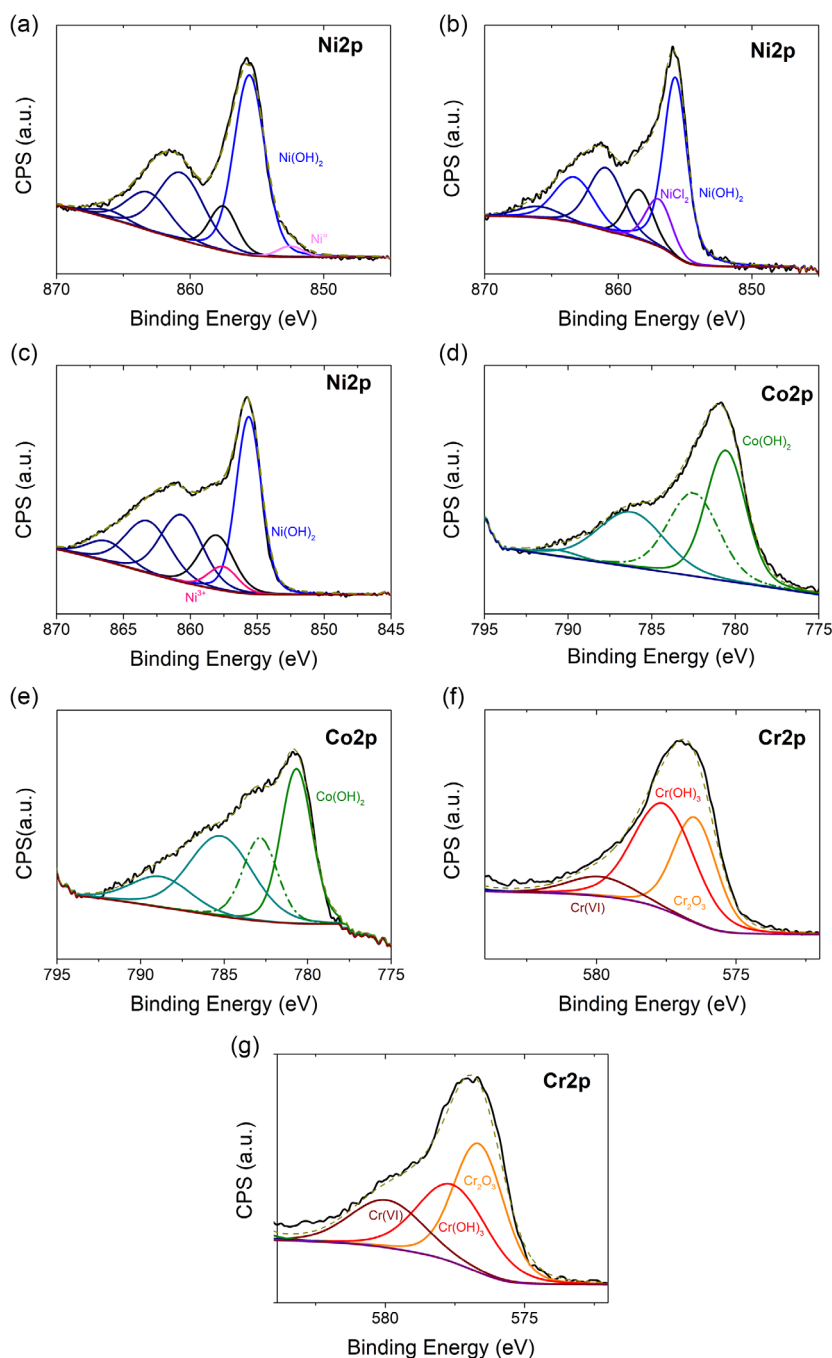


**Figure 8.** Peak-fitted high-resolution core-level spectra for the a–c) Ni2p<sub>3/2</sub>, d,e) Co2p<sub>3/2</sub>, and f,g) Cr2p<sub>3/2</sub> regions of a,d) NiCo, b,f) NiCr and c,e,g) NiCoCr after the electrolytic test at  $-70 \text{ mA cm}^{-2}$  for 10 h.

NiCo and NiCr bimetallic alloys, NiCoCr showed catalytic performance for HER similar to NiCr and higher than that of NiCo, in terms of overpotentials at 10 and  $100 \text{ mA cm}^{-2}$  and Tafel slopes. In contrast, its catalytic activity for OER was quite comparable to that of NiCo and higher than that of NiCr. Importantly, the beneficial role of Cr for OER was clearly demonstrated during controlled-current electrolytic tests for which potential change of only 1 mV was measured after 10 h electrolysis. Globally,

the electrocatalytic performance of NiCoCr for both HER and OER compares well with those of other Ni-based bi- and trimetallic electrocatalysts reported in the literature (Table S5, Supporting Information). Among them, NiCoMo appears to be the most performing alloy based on its HER and OER overpotentials. In our study, the lower catalytic efficiency of NiCoCr is counterbalanced by an excellent stability in OER operation thanks to the presence of Cr. However, it is



worth noticing that performance comparison is not an easy task essentially due to the lack of standardization to report electrochemical data and more specifically electrocatalytic results. Indeed, numerous porous or flat working electrodes have been used (NF, glassy carbon, and metals) and the CV are presented at different scan rates by considering either the geometrical or ECSA.

Moreover, the electrodeposition method investigated herein constitutes a facile and convenient approach to provide cost-effective and durable electrocatalyst for overall electrolytic water splitting. Combining electrodeposition with either surface nanostructuring or the incorporation of heteroatoms in the form of nitrides, sulfides, and borides represents effective strategies to significantly enhance the performance of our bifunctional electrode in order to compete with other highly efficient Ni-based electrocatalysts.

## 4. Experimental Section

**Chemicals:** NF with an average pore size of 350 μm and 1.4 mm thickness was purchased from Recemat B.V. Cell Material Engineering, The Netherlands. KOH was bought from Thermo Fisher Scientific Inc., USA. Ethylenediamine dihydrochloride, chromium (III) chloride hexahydrate were from Sigma-Aldrich and boric acid and nickel (II) chloride hexahydrate were purchased from Alfa Aesar. Cobalt (II) chloride hexahydrate was from Acros Organics. Ultrapure water (Veolia Water-STI) with a resistivity of 18.2 MΩ cm was used to prepare the aqueous solutions and all chemicals were used as received without any further purification.

**Electrodeposition of NiCo, NiCr, and NiCoCr on NF:** Prior to the self-deposition, NF was cleaned with 3 M HCl solution to remove nickel oxide layer,<sup>[49]</sup> ultrapure water, and absolute ethanol under sonication for 10 min in each solution and was dried at 70 °C for 3 h. The deposition solution was obtained by dissolving NiCl<sub>2</sub>, CoCl<sub>2</sub>, CrCl<sub>3</sub>, NH<sub>2</sub>CH<sub>2</sub>CH<sub>2</sub>NH<sub>2</sub>·2HCl, and H<sub>3</sub>BO<sub>3</sub> in ultrapure water. Compositions and concentrations of the baths are given in Table S1, Supporting Information. All the electrodeposited materials were rinsed several times with ultrapure water and then dried under a stream of argon. The electrodeposition was performed using a home-made glass cell, a KCl-saturated Ag/AgCl reference electrode (Metrohm), and a graphitic carbon rod as the counter electrode.

**Instrumentation:** SEM images and elemental mapping were performed using an IT-300 JEOL microscope and an X-Max 50 mm<sup>2</sup> EDX detector (Oxford Instruments).

XRD patterns of synthesized materials on NF were obtained using a Bruker D8 Advance diffractometer (Cu Kα<sub>1</sub> radiation, λ = 1.5406 Å) equipped with a LynxEye fast detector.

XPS data were collected by a Kratos Axis Nova spectrometer using the Al Kα X-Ray source working at 1486.6 eV and using a spot size of 0.7 × 0.3 mm<sup>2</sup>. Survey spectra (0–1000 eV) were acquired with an analyzer pass energy of 160 eV (0.5 eV step<sup>-1</sup>); high-resolution spectra used a pass energy of 40 eV (0.1 eV step<sup>-1</sup>). Binding energies were referenced to C1s peak at 285 eV. The core-level spectra were peak-fitted using the CasaXPS Software, Ltd. Version 2.3.18. U2 Tougaard or Shirley were used as background. The peaks areas were normalized by the manufacturer-supplied sensitivity factor (S<sub>C1s</sub> = 1, S<sub>O1s</sub> = 2.93, S<sub>Cr2p</sub> = 11.67, S<sub>Co2p3/2</sub> = 12.62, S<sub>Ni2p3/2</sub> = 14.61). For each sample, XPS survey spectra were recorded at three different locations, and any differences were not observed.

The electrodeposition and electrochemical measurements were performed at room temperature on a HTDS PARSTAT PMC-200 multichannel electrochemical workstation equipped with an AC frequency response analyzer. Modified NF was directly used as the working electrode (geometric surface area: 1 cm<sup>2</sup>) and a graphite rod was used as the counter electrode. The reference electrode was either 0.1 M KOH-filled Hg/HgO from Orignalys for chronopotentiometry or KCl-saturated Ag/AgCl for cyclic voltammetry. All CVs were Ohmic drop corrected. The Ohmic drop was

determined before each experiment at −0.1 V versus RHE for HER and 1.6 V versus RHE for OER by measuring the impedance of the system at 100 kHz using a 10 mV perturbation. The corresponding Tafel slopes were determined from the linear overpotential versus log (current density) ( $\eta$  vs log  $j$ ) plots. The current densities were normalized by the geometric surface area of the 3D self-supported NF electrodes and all the measured potentials were converted versus the RHE according to the equations given below.

In an alkaline medium (1.0 M KOH, pH = 14 ± 0.1) using a Hg/HgO reference electrode (filled with 0.1 M KOH solution)

$$E_{\text{RHE}} = E_{\text{Hg/HgO}} + 0.059\text{pH} + E^{\circ}_{\text{Hg/HgO}} = E_{\text{Hg/HgO}} + 0.98\text{V} \quad (1)$$

In an alkaline medium (1.0 M KOH, pH = 14 ± 0.1) using an Ag/AgCl reference electrode (filled with saturated KCl solution)

$$E_{\text{RHE}} = E_{\text{Ag/AgCl}} + 0.059\text{pH} + E^{\circ}_{\text{Ag/AgCl}} = E_{\text{Ag/AgCl}} + 1.04\text{V} \quad (2)$$

where  $E_{\text{Hg/HgO}}$  and  $E_{\text{Ag/AgCl}}$  are the applied potential values versus the selected reference electrode.

To calculate the double-layer capacitance ( $C_{\text{dl}}$ ), CVs were recorded in the non-Faradaic region at different scan rates.  $C_{\text{dl}}$  (in mF cm<sup>-2</sup>) corresponds to the slope of the  $\Delta j/2$  vs  $\nu$  plots where  $\Delta j$  is the difference between the anodic and cathodic charging current densities and  $\nu$  is the potential scan rate. The long-term stability of the catalytic electrodes was examined using chronopotentiometry at an applied ±100 mA cm<sup>-2</sup> current density.

## Supporting Information

Supporting Information is available from the Wiley Online Library or from the author.

## Acknowledgements

The scanning electron microscopy and X-ray photoelectron spectroscopy measurements have been performed on CMEBA platforms (ScanMAT, UAR 2025 University of Rennes-CNRS; CPER-FEDER 2015-2020) and at the Institute of Materials of Nantes, respectively. The authors are grateful to Jonathan Hamon (IMN, University of Nantes) for his assistance in X-ray photoelectron spectroscopy experiments. Loïc Joanny and Francis Gouttefangeas are fully acknowledged for scanning electron microscopy images and energy-dispersive X-ray spectroscopy analyses performed at CMEBA (ScanMAT, University of Rennes).

## Conflict of Interest

The authors declare no conflict of interest.

## Author Contributions

B.F. and J.T. conceived the project, designed the experiments, analyzed the data, and wrote the manuscript. C.L. performed and analyzed the X-ray photoelectron spectroscopy data. All authors contributed to Results and Discussion. All authors participated in editing the paper and have given approval to the final version of the manuscript.

## Data Availability Statement

The data that support the findings of this study are available from the corresponding author upon reasonable request.

## Keywords

alkaline electrolysis, hydrogen evolution reactions, oxygen evolution reactions, water splitting

Received: July 11, 2023

Revised: October 9, 2023

Published online: November 22, 2023

- [1] N. S. Lewis, D. G. Nocera, *Proc. Natl. Acad. Sci. U S A* **2006**, *103*, 15729.
- [2] H. Ghahraloud, M. Farsi, M. R. Rahimpour, *Ind. Eng. Chem. Res.* **2018**, *57*, 14114.
- [3] J. Tourneur, B. Fabre, G. Loget, A. Vacher, C. Mériadec, S. Ababou-Girard, F. Gouttefangeas, L. Joanny, E. Cadot, M. Haouas, N. Leclerc-Laronze, C. Falaise, E. Guillon, *J. Am. Chem. Soc.* **2019**, *141*, 11954.
- [4] J. Cao, H. Li, J. Pu, S. Zeng, L. Liu, L. Zhang, F. Luo, L. Ma, K. Zhou, Q. Wei, *Int. J. Hydrogen Energy* **2019**, *44*, 24712.
- [5] Y.-C. Zhang, C. Han, J. Gao, L. Pan, J. Wu, X.-D. Zhu, J.-J. Zou, *ACS Catal.* **2021**, *11*, 12485.
- [6] S. Trasatti, *J. Electroanal. Chem. Interfacial Electrochem.* **1972**, *39*, 163.
- [7] I. A. Raj, K. I. Vasu, *J. Appl. Electrochem.* **1990**, *20*, 32.
- [8] I. Roger, M. A. Shipman, M. D. Symes, *Nat. Rev. Chem.* **2017**, *1*, 0003.
- [9] F. Ganci, B. Patella, E. Cannata, V. Cusumano, G. Aiello, C. Sunseri, P. Mandin, R. Inguanta, *Int. J. Hydrogen Energy* **2021**, *46*, 35777.
- [10] F. Ganci, V. Cusumano, P. Livreri, G. Aiello, C. Sunseri, R. Inguanta, *Hydrogen Fuel Cells* **2021**, *46*, 10082.
- [11] C. C. L. McCrory, S. Jung, I. M. Ferrer, S. M. Chatman, J. C. Peters, T. F. Jaramillo, *J. Am. Chem. Soc.* **2015**, *137*, 4347.
- [12] Y. Hu, J. Xu, T. Zhang, H. Zhong, J. Chen, X. Liu, Q. Pan, R. Liu, C. Jiang, J. Chen, *Transition. Met. Chem.* **2023**, *48*, 125.
- [13] Gh. B. Darband, M. Aliofkhaezrai, A. S. Rouhaghdam, *J. Colloid Interface Sci.* **2019**, *547*, 407.
- [14] V. Bachvarov, E. Lefterova, R. Rashkov, *Int. J. Hydrogen Energy* **2016**, *41*, 12762.
- [15] S. M. N. Jeghan, N. Kim, G. Lee, *Int. J. Hydrogen Energy* **2021**, *46*, 22463.
- [16] D. Maarisetty, D.-R. Hang, M. M. C. Chou, S. Parida, *ACS Appl. Energy Mater.* **2022**, *5*, 14059.
- [17] H. Nady, M. M. El-Rabiei, M. Samy, M. A. Deyab, G. M. Abd El-Hafez, *Int. J. Hydrogen Energy* **2021**, *46*, 34749.
- [18] C.-T. Hsieh, C.-L. Huang, Y.-A. Chen, S.-Y. Lu, *Appl. Catal., B* **2020**, *267*, 118376.
- [19] M. Baek, G.-W. Kim, T. Park, K. Yong, *Small* **2019**, *15*, 1905501.
- [20] Y. Yang, L. Dang, M. J. Shearer, H. Sheng, W. Li, J. Chen, P. Xiao, Y. Zhang, R. J. Hamers, S. Jin, *Adv. Energy Mater.* **2018**, *8*, 1703189.
- [21] A. Nairan, P. Zou, C. Liang, J. Liu, D. Wu, P. Liu, C. Yang, *Adv. Funct. Mater.* **2019**, *29*, 1903747.
- [22] F. Bao, E. Kemppainen, I. Dorbandt, F. Xi, R. Bors, N. Maticiuic, R. Wenisch, R. Bagacki, C. Schary, U. Michalczyk, P. Bogdanoff, I. Lauer mann, R. van de Krol, R. Schlattmann, S. Calnan, *ACS Catal.* **2021**, *11*, 10537.
- [23] C. Feng, M. B. Faheem, J. Fu, Y. Xiao, C. Li, Y. Li, *ACS Catal.* **2020**, *10*, 4019.
- [24] S. P. Babu, A. Falch, *ChemCatChem* **2022**, *14*, e202200364.
- [25] L. Peng, J. Min, A. Bendavid, D. Chu, X. Lu, R. Amal, Z. Han, *ACS Appl. Mater. Interfaces* **2022**, *14*, 40822.
- [26] H.-W. Hsiao, R. Feng, H. Ni, K. An, J. D. Poplawsky, P. K. Liaw, J.-M. Zuo, *Nat. Commun.* **2022**, *13*, 6651.
- [27] G. Laplanche, A. Kostka, C. Reinhart, J. Hunfeld, G. Eggeler, E. P. George, *Acta Mater.* **2017**, *128*, 292.
- [28] B. Gludovatz, A. Hohenwarter, K. V. S. Thurston, H. Bei, Z. Wu, E. P. George, R. O. Ritchie, *Nat. Commun.* **2016**, *7*, 10602.
- [29] R. Giovanardi, G. Orlando, *Surf. Coat. Technol.* **2011**, *205*, 3947.
- [30] C. Xu, P. Chen, B. Hu, Q. Xiang, Y. Cen, B. Hu, L. Liu, Y. Liu, D. Yu, C. Chen, *CrystEngComm* **2020**, *22*, 4228.
- [31] A. P. Grosvenor, M. C. Biesinger, R. St.C. Smart, N. S. McIntyre, *Surf. Sci.* **2006**, *600*, 1771.
- [32] M. C. Biesinger, B. P. Payne, L. W. M. Lau, A. Gerson, R. St.C. Smart, *Surf. Interface Anal.* **2009**, *41*, 324.
- [33] M. C. Biesinger, B. P. Payne, A. P. Grosvenor, L. W. M. Lau, A. R. Gerson, R. St.C. Smart, *Appl. Surf. Sci.* **2011**, *257*, 2717.
- [34] X. Wang, J. Hu, Y. Su, J. Hao, F. Liu, S. Han, J. An, J. Lian, *Chem. – Eur. J.* **2017**, *23*, 4128.
- [35] M. C. Biesinger, L. W. M. Lau, A. R. Gerson, R. St.C. Smart, *Phys. Chem. Chem. Phys.* **2012**, *14*, 2434.
- [36] H. A. E. Hagelin-Weaver, J. F. Weaver, G. B. Hoflund, G. N. Salaita, *J. Electron Spectrosc. Relat. Phenom.* **2004**, *134*, 139.
- [37] H. A. E. Hagelin-Weaver, J. F. Weaver, G. B. Hoflund, G. N. Salaita, *J. Alloys Compd.* **2005**, *389*, 34.
- [38] F. Armillotta, D. Bidoggia, P. Biasin, A. Annese, A. Cossaro, A. Verdini, L. Floreano, M. Peressi, E. Vesselli, *Cell Rep. Phys. Sci.* **2023**, *4*, 101378.
- [39] J. Yang, H. Liu, W. N. Martens, R. L. Frost, *J. Phys. Chem. C* **2010**, *114*, 111.
- [40] S. Hesamedini, G. Ecke, A. Bund, *J. Electrochem. Soc.* **2018**, *165*, C657.
- [41] J. Li, C. Yao, Y. Liu, D. Li, B. Zhou, W. Cai, *J. Hazard. Mater.* **2012**, *221–222*, 56.
- [42] D. S. Hall, C. Bock, B. R. MacDougall, *J. Electrochem. Soc.* **2013**, *160*, F235.
- [43] Z. Yu, Y. Duan, X. Feng, X. Yu, M. Gao, S. Yu, *Adv. Mater.* **2021**, *33*, 2007100.
- [44] S. L. Medway, C. A. Lucas, A. Kowal, R. J. Nichols, D. Johnson, *J. Electroanal. Chem.* **2006**, *587*, 172.
- [45] L. Trotochaud, J. K. Ranney, K. N. Williams, S. W. Boettcher, *J. Am. Chem. Soc.* **2012**, *134*, 17253.
- [46] D. K. Bediako, B. Lassalle-Kaiser, Y. Surendranath, J. Yano, V. K. Yachandra, D. G. Nocera, *J. Am. Chem. Soc.* **2012**, *134*, 6801.
- [47] S. Trasatti, O. A. Petrii, *J. Electroanal. Chem.* **1992**, *327*, 353.
- [48] A. Peugeot, C. E. Creissen, M. W. Schreiber, M. Fontecave, *ChemElectroChem* **2022**, *6*, e202200148.
- [49] S. A. Ansari, N. Parveen, M. A. Al-Othoum, M. O. Ansari, *Nanomaterials* **2021**, *11*, 1596.